THE JOURNAL OF PHYSICAL CHEMISTRY B

Article

pubs.acs.org/JPCB

Structure and Aggregation in the 1-Alkyl-3-Methylimidazolium Bis(trifluoromethylsulfonyl)imide Ionic Liquid Homologous Series

Karina Shimizu,[†,‡] Carlos E. S. Bernardes,[†] and José N. Canongia Lopes*[,†,‡]

[†]Centro de Química Estrutural, Instituto Superior Técnico, 1049-001 Lisboa, Portugal

[‡]Instituto de Tecnologia Química e Biológica, Universidade Nova de Lisboa, Avenida República, 2780-157 Oeiras, Portugal

ABSTRACT: A new comprehensive Molecular Dynamics study using large simulation boxes has been performed in order to complete and extend the structural analysis on the mesoscopic segregation observed in the ionic liquids of the 1-alkyl-3-methylimidazolium bis(trifluoromethylsulfonyl)imide homologous series, $[C_nC_1im][Ntf_2]$ ($2 \leq n \leq 10$). The analysis includes the discussion along the whole family of the corresponding structure factors, $S(q)$, in the low-q range ($1.6 \leq q/nm^{-1} \leq 20$); the confirmation of the periodicity of the polar network of the ionic liquid and its intermediate low-q peak equivalence; and the introduction of five statistical functions that probe the existence and characterize the polar network and the nonpolar aggregates that are formed along the $[C_nC_1im][Ntf_2]$ series. The later functions comprise aggregate size distributions, average number of contact neighbors within an aggregate, neighbor distributions, distributions of aggregate maximum length, and distributions of aggregate volume.

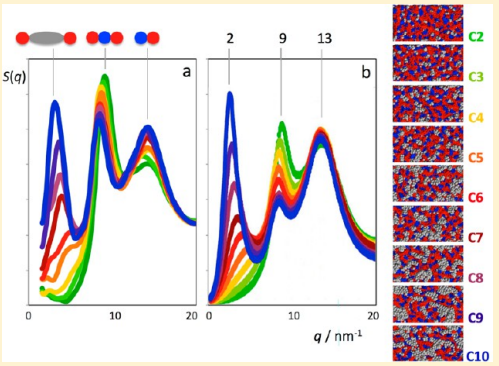

INTRODUCTION

The notion that the structure of ionic liquids (ILs) is complex and can exhibit nanoscale segregation started to be investigated almost 10 years ago via molecular modeling studies.[1−3] The existence of mesoscopic structures composed by the different moieties that are part of the molecular ions of some ionic liquids was confirmed experimentally in 2007 by X-ray diffraction[4] and the interpretation of the corresponding spectra has been an area of intense debate since then.[5−18] Experimental evidence linking the structure of ILs to their macroscopic properties has also been interpreted in terms of the underlying nanoscale segregation.[19−21]

One of the central guidelines in most of these investigations has been the use of homologous series of ionic liquids—where the alkyl side chain attached to one of the ionic species is slowly increased—to explore in a systematic way the effect of the ratio between polar and nonpolar ionic moieties on the IL structure. In this context, the 1-alkyl-3-methylimidazolium bis(trifluoromethylsulfonyl)imide series, $[C_nC_1im][Ntf_2]$ (cf. scheme 1), has been one of the preferred choices for both experimental and theoretical studies.

In this article we will revisit the $[C_nC_1im][Ntf_2]$ series and extend the analysis of its mesoscopic structure in order to encompass both a more detailed and complete description of the structure factors along the homologous series and also a novel approach based on the interconnectivity between the different ionic species and the corresponding aggregation into clusters of different morphology.

EXPERIMENTAL SECTION

Molecular Dynamics Simulation. All members of the $[C_nC_1im][Ntf_2]$ series with n between 2 and 10 were modeled using the previously reported CL&P atomistic force field.[22−24] The CL&P force field is an extension of the AMBER/OPLS force fields[25] specially designed to encompass whole families of ionic liquids in a systematic way.

The molecular dynamics simulations were carried out with the DL_POLY 2.20 package.[26] A cutoff distance of 1.6 nm was selected in all calculations, with the Ewald summation technique applied to account for interactions beyond that distance. The simulations were performed at a pressure of 0.1 MPa at 298 K, under the isotropic isothermal−isobaric ensemble (N-p-T), by using a Nosé−Hoover thermostat and barostat with relaxation time constants of 1 and 4 ps, respectively. In all runs, a time step of 2 fs was used.

Two sets of simulations were performed. The first set comprised simulation boxes with 200 ion pairs of each ionic liquid. All these simulations started from low-density configurations and/or from previously equilibrated simulation boxes used in previous works.[19] All initial boxes (including the pre-equilibrated ones) were subjected to four-stage equilibration runs, where the pressure and temperature were changed according to the following sequence: (*i*) 1.0 ns at p = 5.0 MPa, T = 1000 K; (*ii*) 1.0 ns at p = 0.1 MPa, T = 1000 K; (*iii*) 1.0 ns at p = 0.5 MPa, T = 298 K; (*iv*) 3.0 ns at p = 0.1 MPa, T = 298 K. After repeating this sequence several times, the density of

Received: October 8, 2013
Revised: November 20, 2013
Published: December 20, 2013

Scheme 1. Schematic Representation and Nomenclature Used Throughout the Text of the Ions of the $[C_nC_1im][Ntf_2]$ Series[a]

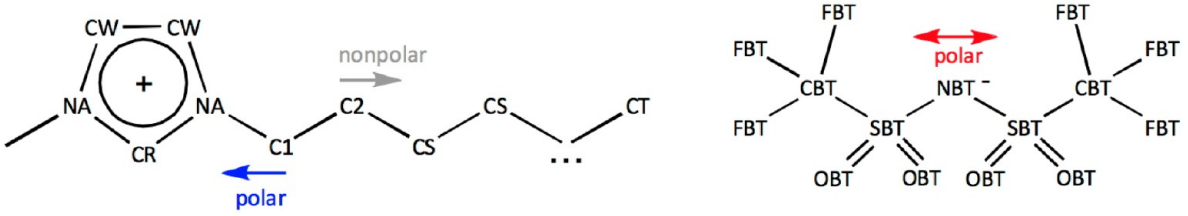

[a]The arrows/colors indicate the parts of the molecular ions that are differentiated in the color-coded simulation snapshots in Figure 3.

each system reached constant and consistent values, indicating that an equilibrium state had been attained and possible ergodicity problems had been overcome. Finally, several (ranging from 5 to 10) consecutive production stages of 1.0 ns each were performed, and the obtained results were used for the molecular aggregation analyses (see below).

The second set of simulations were performed using simulation boxes composed by 1600 ion pairs. The larger simulation boxes were created by stacking eight cubic simulation boxes containing the final equilibrated configurations obtained in the previous set in order to generate 2 × 2 × 2 simulation boxes. The initial configurations thus obtained were then re-equilibrated/relaxed for 0.1 ns at p = 0.1 MPa, T = 298 K. This was followed by several consecutive (5−15) production stages of 0.1 ns each under the same temperature and pressure conditions. The production data were used to calculate the structure factors of the corresponding fluids.

Structure Factors. The total static structure factors, $S(q)$, were calculated using the a previously described methodology.[27] In brief, $S(q)$ was obtained from

$$S(q) = \sum_i \sum_j S_{ij}(q) \tag{1}$$

$$S_{ij}(q) = \frac{\rho_o x_i x_j b_i(q) b_j(q) \int_0^R 4\pi r^2 [g_{ij}(r) - 1] \frac{\sin(qr)}{qr} \frac{\sin(\pi R)}{\pi r / R} dr}{(\sum_i x_i b_i(q))^2} \tag{2}$$

where $S_{ij}(q)$ is the partial static structure factor between atoms of type i and j (e.g., carbon, hydrogen or nitrogen), calculated from the corresponding Fourier transform of the partial radial distribution function $g_{ij}(r)$; q is the scattering vector; ρ_o is the average atom number density; R is the cutoff used in the calculation of $g_{ij}(r)$, established to half the side of the simulation box (in this case it varied between 4.2 and 5.0 nm for the ionic liquids comprised between $[C_2C_1im][Ntf_2]$ to $[C_{10}C_1im][Ntf_2]$, respectively); x_i and x_j are the atomic fraction of i and j; and $b_i(q)$ and $b_j(q)$ are the coherent bound neutron scattering length of the corresponding atom type, interpolated from recommended values in the International Tables for Crystallography.[28] The term $\sin(\pi R)/(\pi r/R)$ in eq 2 is a Lorch type window function used to reduce the effect of using a finite cutoff in the radial distribution function calculation.[29]

Aggregation Analysis. The structural analyses of the $[C_nC_1im][Ntf_2]$ ionic liquids—the evaluation of the connectivity between ion contact pairs or different moieties of the molecular ions—were based on the previously described algorithms used in a study of aggregates in solution.[30]

In the case of the connectivity within the IL polar networks, no modification to the original programs was performed. For the present ionic liquids, it was considered that the center of negative charge of the anions was formally located in the nitrogen atom of the $[Ntf_2]^-$ ion, NBT, whereas the positive charge of the cation was located in the center-of-mass of the imidazolium ring. An interionic distance of 0.8 nm between these two centers was then considered as the first coordination shell limit and thus, the limiting distance for an anion and a cation to form a contact ion pair. The use of this criterion allowed the computation of closest neighbor lists for each cation or anion (composed exclusively by counterions) for every recorded configuration in the production runs, thus ascertaining the connectivity within the polar network and the characteristics of the corresponding polar network. The cutoff distance of 0.8 nm was established based on analyses of the radial distribution functions (RDFs) between the two aforementioned charge centers (Figure 1a). Due to the difficulty in the evaluation of the first coordination shell limit, the first peak of the RDF was deconvoluted and the largest Gaussian curve was then considered to represent the main interaction between the cation and anion interaction centers; the distance at which it vanished was then considered as the reference distance (cf. Figure 1a).

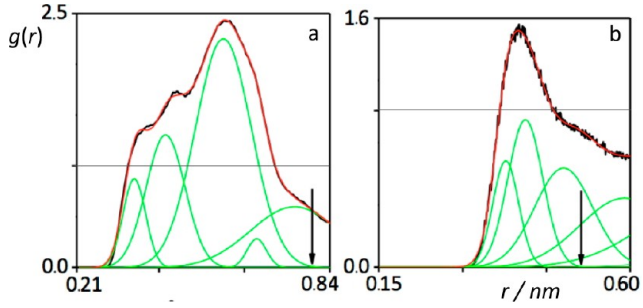

Figure 1. Radial distribution functions (RDFs) used in the determination of the connectivity criteria for the aggregation analyzes. (a) RDF between the center-of-mass of the imidazolium ring and the nitrogen atom of the anion (NBT); (b) RDF between the terminal carbon atoms (CT) of the imidazolium alkyl chains. Both RDFs where obtained for $[C_{10}C_1im][Ntf_2]$. The green curves are the result of the deconvolution of the RDF first peak by using a series of Gaussian functions; the red curves are the resultants of the sum of the corresponding Gaussian functions.

An analogous strategy was used for the study of the nonpolar domains. In this case, however, the connectivity criterion was that two alkyl chains would belong to the same aggregate (nonpolar domain) if the distance between any of the carbon atoms belonging to the alkyl chain (from C2 to CT, cf. Scheme 1) was smaller than 0.5 nm. Similarly to the previous case, this criterion was estimated from the radial distribution functions (RDFs) computed between the terminal carbon atoms (CT) of the alkyl chains of $[C_{10}C_1im]^+$ (Figure 1b), after deconvolution

dx.doi.org/10.1021/jp409987d | J. Phys. Chem. B 2014, 118, 567−576

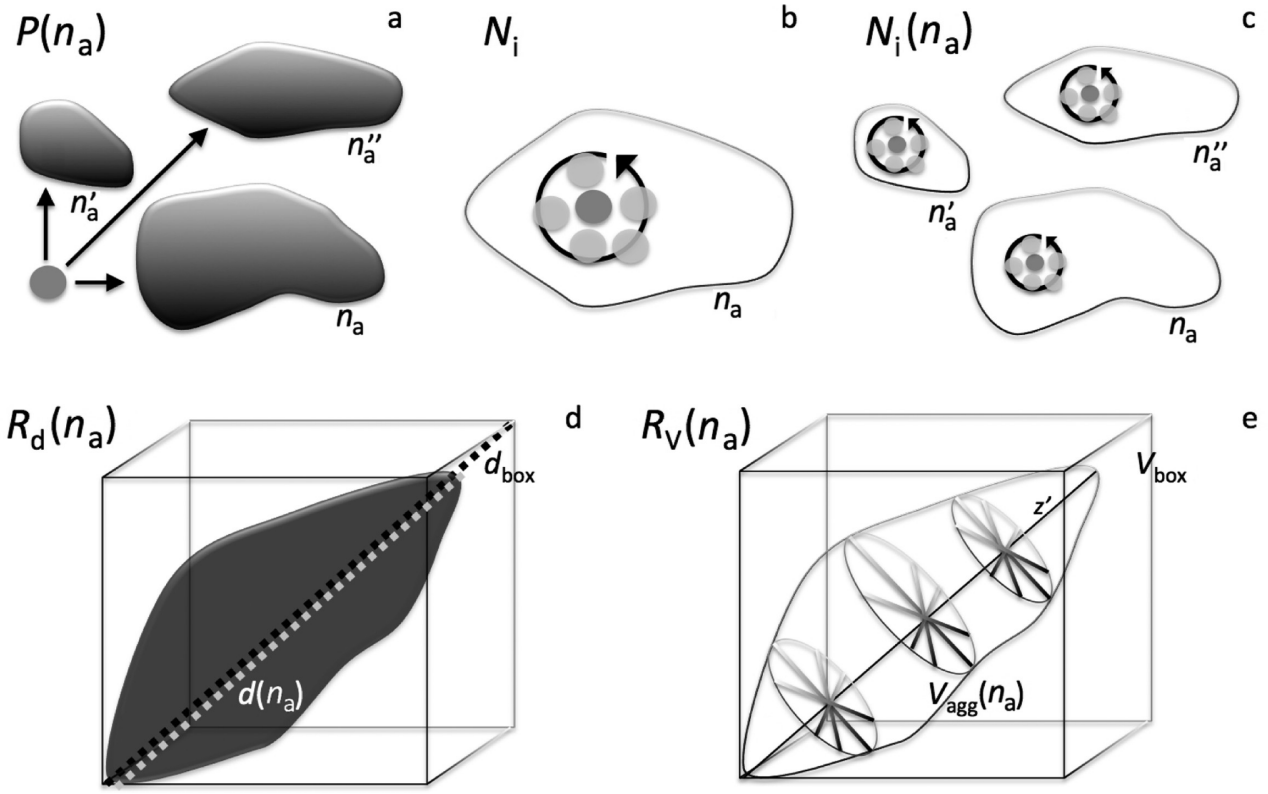

Figure 2. Schematic representation of the five statistical functions that were used in the aggregate analyses of the MD data along the $[C_nC_1im][Ntf_2]$ homologous series. The n_a labels (with different number of primes) refer to aggregates of different sizes.

of the first peak and evaluation of the value at which the main Gaussian curve reached zero. Again, by using the previous condition, the neighbor lists of each alkyl side chain were transformed into connectivity/aggregate lists using the algorithm used for aggregation studies in IL aqueous solutions.[30]

As before,[30] several statistical functions were used to characterize the network/aggregates that emerge from the connectivity lists. These are given by eqs 3−7; their physical/statistical meaning is rendered schematically in Figure 2.

The average aggregate size distribution for a given ionic liquid is expressed by the distribution function

$$P(n_a) = \frac{n_a \sum_{j=1}^{C} A_{n_a}(j)}{C \cdot I} \tag{3}$$

where $P(n_a)$ is the probability of finding a given molecular ion or alkyl side chain in an aggregate of size n_a (a polar network composed by n_a ions or a nonpolar aggregate composed by n_a alkyl chains), C is the total number of configurations acquired during the production stage, $A_{n_a}(j)$ is the number of aggregates of size n_a for a given configuration j, and I is the total number of ions (cations plus anions)/alkyl chains in the simulation box.

The overall average number of neighbors of each species is expressed by

$$N_i = \frac{\sum_{j=1}^{C} V_i(j)}{C \cdot I_i} \tag{4}$$

where $V_i(j)$ is the total number of neighbors (counterions or other alkyl chains) of all ions or alkyl chains of type i for a given configuration j and I_i is the number of ions or alkyl chains of type i in the simulation box.

On the other hand, $N_i(n_a)$ is the average number of neighbors of a given ion or alkyl chain of type i in an aggregate of size n_a, expressed by

$$N_i(n_a) = \frac{\sum_{j=1}^{C} V_{i,n_a}(j)}{\sum_{j=1}^{C} I_i(j)} \tag{5}$$

where $V_{i,na}(j)$ is the total number of neighbors of an ion or alkyl chain of type i in an aggregate of size n_a and $I_i(j)$ is the total number of ions or alkyl chains of type i in all aggregates of size n_a.

Finally, in order to investigate the size and shape of the aggregates, two novel functions were introduced: The average ratio, $R_d(n_a)$, between the longest distance, d, that can be draw between two atoms within the same aggregate of size n_a and the simulation box diagonal, d_{box}, was computed as

$$R_d(n_a) = \frac{\sum_{j=1}^{C} \frac{\sum_{k=1}^{N} \frac{d(k)}{d_{box}}}{N}}{C} \tag{6}$$

where N is the number of aggregates of size n_a in the configuration j; Additionally, the ratio, $R_V(n_a)$, between the apparent volume of an aggregate of size n_a, V_{agg}, and the simulation box volume, V_{box}, was estimated as

$$R_V(n_a) = \frac{\sum_{j=1}^{C} \frac{\sum_{k=1}^{N} \frac{V_{agg}(k)}{V_{box}}}{N}}{C} \tag{7}$$

dx.doi.org/10.1021/jp409987d | J. Phys. Chem. B 2014, 118, 567−576

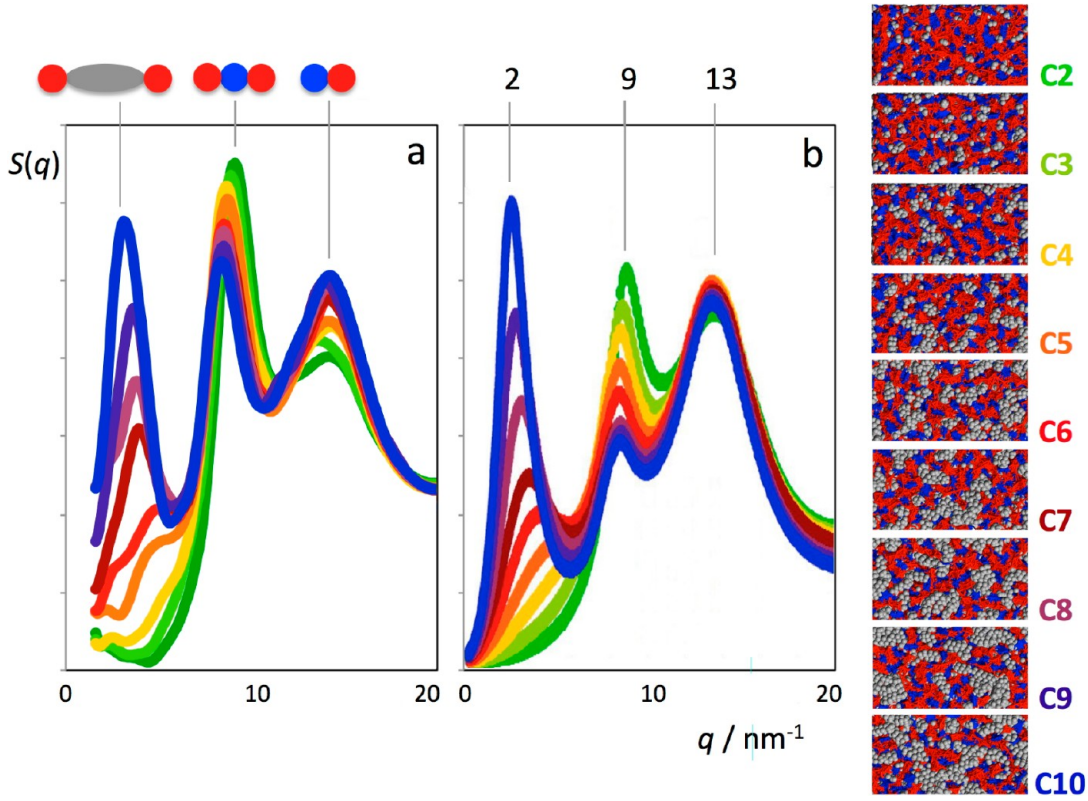

Figure 3. Structure factors, $S(q)$, as a function of reciprocal space wavenumber, q, for the $[C_nC_1im][Ntf_2]$ homologous series. (a) MD simulation data (this work); (b) representation based on the X-ray data from Triolo et al.[34] The simulation snapshots on the right are color-coded to reflect the presence of the charged parts of the cations (blue), the anions (red) and the nonpolar parts (tails) of the cations (gray). The small vignettes above (a) represent structural features assigned to each peak (see text); the numbers above (b) indicate the approximate q-values of each family of peaks.

The longest distance within an aggregate can be easily computed by calculating the largest value of all the distances between atoms belonging to ions/chains that are part of the same aggregate. The apparent volume of an aggregate was calculated using the following method: (*i*) the aggregate was vertically aligned with a reference coordinate system (its longest diagonal, of dimension d_z, was superimposed with a z'-axis and one of its extremities located at the axes origin); (*ii*) 26 grid points located at the surface of the aggregate were computed. These include the two points at the vertical extremities of the aggregate (0, 0, 0) and (0, 0, d_z) plus 24 points at the intercept of the aggregate surface with 12 straight lines resulting from the interception of the three ($z' = d_z/4$, $d_z/2$, and $3d_z/4$ planes) with the four ($x' = 0$, $y' = 0$, $x' = y'$ and $x' = -y'$) planes; (*iii*) finally, the volume of the geometric solid defined by the grid points was computed to find V_{agg}. The procedure just outlined only leads to an approximate estimate for the apparent volume of the aggregates: the 26 points only capture the shape of the aggregate in a coarse way, not accounting for possible concavities, the intermeshing of the polar network with the non polar domains or other structural details at the atomistic level.

RESULTS AND DISCUSSION

1. Structure Factors. As already mentioned in the Introduction, other authors reported structure factors for different IL series obtained experimentally and/or using molecular simulations.[5,31−33] Although the interpretation of the data has been sometimes controversial, the data itself are quite consistent. However, to our knowledge, this is the first report where structure factors with q-values ranging from 1.6 to 20 nm^{-1} for the entire $[C_nC_1im][Ntf_2]$, with all integer n values between 2 and 10, were obtained from MD simulation results and compared to the corresponding experimental X-ray diffraction results.

The structure factors obtained in this work of the nine systems under discussion are plotted in Figure 3 along with a similar plot taken from ref 34 obtained experimentally using X-ray diffraction data. The two plots are also accompanied by nine simulation snapshots highlighting the progressive increase and segregation of the nonpolar domains as the alkyl side chains become larger along the homologous series.

Although the intensity scale of the $S(q)$ plots is arbitrary and the fluctuations of the MD plots for lower q values are dependent on the size of the simulation boxes and the corresponding boundary conditions (hence the use of particularly large simulation boxes and the absence of MD $S(q)$ data for $q < 1.6$ nm^{-1}), the trends along each plot are strikingly similar.

In both plots the $[C_{10}C_1im][Ntf_2]$ spectra exhibits three well-defined peaks around (*i*) 13, (*ii*) 9, and (*iii*) 2 nm^{-1}, and these have been identified[5] (for similar ILs based on the same cation combined with the hexafluorphosphate anion) with length scales associated with (*i*) cation−anion direct contact pairs, (*ii*) closest cation−cation or anion−anion distances within the polar network, and (*iii*) ion−ion distances mediated by nonpolar domains. In the present context, "ion-ion distances" mean the distances between the charged parts of the ions, cf. Scheme 1. These contributions are represented as vignettes superimposed in Figure 3a. It must also be stressed

dx.doi.org/10.1021/jp409987d | J. Phys. Chem. B 2014, 118, 567−576

that it was also shown[5] that the aforementioned peaks are the sum of contributions from different pair correlations with different signs and amplitudes. Specially in the case of the peak in the 13 nm^{-1} region, other inter- and intramolecular correlation distances also contribute to the peak. This means that it is difficult on one hand to assign a peak to a characteristic distance between a particular pair of atomic centers, and, on the other hand, to describe the relative intensities and trends between peaks, including the appearance of shoulders or other less conspicuous features. Nevertheless, as one moves within the $[C_nC_1im][Ntf_2]$ series, the intensities of the three peaks shift in a regular manner, both for the MD and X-ray results, and it is possible to infer some results that can then be confirmed by further structural analyses (see next section).

The most conspicuous trend is that of the so-called prepeak centered around 2−3 nm^{-1}. This peak is not present for the smaller ILs (from $[C_2C_1im][Ntf_2]$ to $[C_4C_1im][Ntf_2]$), is a shoulder or an incipient peak for $[C_5C_1im][Ntf_2]$ and $[C_6C_1im][Ntf_2]$, respectively, and shows increasingly larger intensities from $[C_7C_1im][Ntf_2]$ to $[C_{10}C_1im][Ntf_2]$. This fact has been associated with the emergence of a bicontinuous mesoscopic phase for the larger members of the $[C_nC_1im][Ntf_2]$ series (C7−C10), triggered around $[C_5C_1im][Ntf_2]$ by the percolation of the small and disperse alkyl chain aggregates that exist in the shorter members of the $[C_nC_1im][Ntf_2]$ series (C2−C4).[19,33] The shift of the prepeak to smaller q values (corresponding to larger distances in normal space) as the alkyl side chains increase in length can also be associated to the increase in size of the nonpolar subphases (not only length but also width, cf. aggregate analysis below) along the C2−C10 series.

The intermediate peak centered around 9 nm^{-1} also exhibits a intensity shift along the series but in reverse order relative to the trend observed for the prepeak. On the other hand, the q-value shifts of the intermediate peak along the series are in the same direction of those of the prepeak. It must be stressed that the intermediate and the larger-q peaks (centered at 9 and 13 nm^{-1}, respectively) are correlated—they stand for characteristic wavenumbers associated to the polar network of the ionic liquid and, in fact, for some ILs, one of the peaks is present only as a shoulder of the more prominent peak. This means that any analyses should be performed with special care since q-value shifts in one of the peaks may only reflect intensity shifts in the other peak and not a change in a characteristic length of the system. Nevertheless, in the present case, both the experimental X-ray diffraction data (Figure 3b) and the MD results (Figure 3a) relative to the intermediate peak seem to point in the same direction: weaker correlations and slightly larger characteristic distances between ions of the same sign within the polar network as the alkyl side chains become longer. These results are consistent with the fact that the polar network must be partially broken (although without loosing its three-dimensional continuity) in order to accommodate progressively larger nonpolar domains. This has an impact on the number of counterions present in the first-shell of a given ion (cf. aggregate analyses below) and an even bigger effect on the number of second-shell (same-charge) ions and can explain the intensity decrease of the intermediate peak along the C2−C10 series. On the other hand, the gradual transformation of the polar network, from a more or less isotropic/globular arrangement (cf. top snapshot of Figure 3 for $[C_2C_1im][Ntf_2]$) to a more or less sponge-like structure (cf. bottom snapshot of Figure 3 for $[C_{10}C_1im][Ntf_2]$), can explain the shifts of the intermediate peak to smaller q values: if the charged parts of the ions are confined to more elongated structures in the sponge-like polar networks of the larger ILs, the proportion of (ion)−(counterion)−(ion) angles closer to 180° becomes larger and the corresponding (ion)−(ion) distances increase.

In the case of the peak centered at 13 nm^{-1} (that has contributions from correlations between direct contacts between ions of opposite sign), both the MD and diffraction results show no q-shifts—the direct contact pair (ion)−(counterion) distances are unaffected by the presence of the nonpolar domains—and a modest increase in the (ion)−(counterion) correlations. This seems to contradict the decrease in the number of first-shell neighbors that is expected along the C2−C10 series. However, one has to be reminded that even if there is a decrease in the number of first-shell neighbors, that decrease is limited by the fact that each ion center will strive to maintain local electroneutrality conditions and the continuity of the polar network. In other words, as the alkyl side chains become longer, the ions do not get "diluted" in an uniform way in the nonpolar domains but rather form a different (more open) polar network. In this context—if one takes into account the dilution effect caused by the space that is now being occupied by the nonpolar domains—the correlation between direct ion pairs can in fact be enhanced. As we have discussed above, the same does not apply to the correlations between the second-shell neighbors in the polar network. Both the MD and X-ray results show these reverse correlation trends between the intermediate and the higher-q peak that characterize the polar network.

Finally, the presence of a continuous polar network throughout the IL homologous series—as attested by the persistence of the two $S(q)$ peaks just discussed—can also be analyzed in direct space using the corresponding (ion)−(counterion) and (ion)−(ion) radial distribution functions (RDFs), presented in Figure 4 for three selected ILs. The opposition-of-phase character of such representations can be thought of as the "fingerprint" of an ionic liquid or a molten salt and has been frequently used in recent times[35] to show why an ionic fluid—that must fulfill local electroneutrality conditions—will always have some degree of medium-range ordering. In the present case, the use of large simulation boxes (cubes with sides greater than 8 nm) allowed the extension of the RDF length limits up to more than 4 nm and enabled the comparison of the different polar networks along the IL series. Such extended RDFs show the large number of shells of alternating charge surrounding a particular ion—10 such shells can be easily counted for $[C_2C_1im][Ntf_2]$ or 8 for $[C_6C_1im][Ntf_2]$ and $[C_{10}C_1im][Ntf_2]$ (cf. Figure 4 insets)—and can also be associated to the intermediate peak in reciprocal space: q-values of 9.1, 8.6, and 8.4 nm^{-1} taken from the $S(q)$ functions (intermediate peak) for $[C_2C_1im][Ntf_2]$, $[C_6C_1im][Ntf_2]$, and $[C_{10}C_1im][Ntf_2]$, respectively (Figure 3a) were used to calculate distances in direct space corresponding to 0.69, 0.73, and 0.75 nm. These are depicted in Figure 4 as the distances between the colored gridlines delimiting the wavelengths of the alternating RDFs. The gridlines show that as the nonpolar domains increase in size along the IL series, the polar network will persist but will have to accommodate the growing nonpolar domains by loosing part of its connectivity (and becoming more disordered at longer distances, cf. Figure4 and aggregate analyses section below) but also by slightly stretching itself (ionic layers with greater wavelength values, intermediate peak shifts to smaller q-values). In this context,

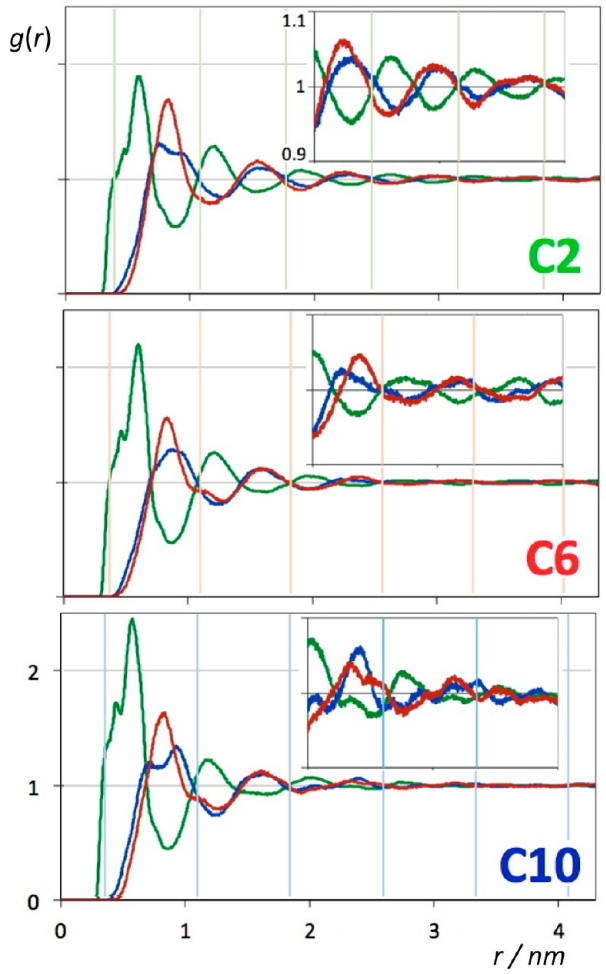

Figure 4. Three selected radial distribution functions (RDFs), $g(r)$, as a function of distance, r, for three selected ILs in the $[C_nC_1im][Ntf_2]$ homologous series. Green lines: RDFs between selected positions in the cation (imidazolium ring centroid) and anion (NBT atom, cf. Scheme 1); blue lines: RDFs between imidazolium ring centroids; red lines: RDFs between NBT atoms. The colored vertical lines reflect the wavelength of the RDFs in each case and are related to the position of the corresponding intermediate q-peaks in Figure 3. The insets vertically magnify the region between 2 and 4 nm.

one can speculate that the existence of large and flexible anions such as $[Ntf_2]^-$ or cations with charge-delocalized rings such as $[C_nC_1im]^+$ can play an important role in such stretching-without-rupture processes: as the polar network swells, the ions can adopt different conformations or relative configurations that enable them to interact equally well with different counterions at slightly longer distances. In fact, the structure of the first peak of the (cation)−(cation) RDFs (blue curves in Figure 4) are due to different possible relative configurations of two imidazolium rings relative to each other. In this context it is relevant that as the polar network stretches, the peak-shoulder structure observed in $[C_2C_1im][Ntf_2]$ evolves to the shoulder-peak structure found for $[C_{10}C_1im][Ntf_2]$.

2. Aggregate Analysis. In this section we will use the different statistical tools introduced in the Experimental Section to analyze the aggregation patterns that emerge throughout the $[C_nC_1im][Ntf_2]$ series. As mentioned before, the simulation boxes used for this part of the work are smaller than those used to obtain the $S(q)$ data. This means that aggregates containing 200 ion pairs or 200 alkyl side chains comprise all ions/chains in the simulation boxes. The first issue to be considered will be the distribution of aggregate sizes, $P(n_a)$, along the series.

As mentioned in the last couple of paragraphs of the previous section, the polar network is ubiquitous for $[C_2C_1im][Ntf_2]$ and is stretched/broken but still continuous for $[C_{10}C_1im][Ntf_2]$. The calculation of $P(n_a)$ for the ionic part of all ILs under discussion, has yielded $P(200) \approx 1$ and $P(<200) \approx 0$. This confirms that even for $[C_{10}C_1im][Ntf_2]$, a given ion is almost always part of an aggregate that contains all other ions present in the simulation box, i.e., there are no isolated fragments of the polar network; there is only one large aggregate (that is generally dubbed *the* polar network).

Things are drastically different if we consider the nonpolar moieties of the cations (for tallying purposes, the polar to nonpolar transition within the $[C_nC_1im]^+$ cation was established between the methylene group connected directly to the imidazolium ring and the following group along the chain; cf. Scheme 1). In this case, the aggregate distributions, $P(n_a)$ for the alkyl side chains of the $[C_nC_1im]^+$ cations vary a lot along the series, as can be seen by the distribution functions depicted in Figure 5.

In $[C_2C_1im][Ntf_2]$, some 40% of the chains (in this case just the terminal CH_3 group of the ethyl chain) are isolated in the midst of the polar network, some 25% of them are paired, 15% form trios, and very few aggregate "islands" with more than 10 tails were observed. As one progresses from $[C_2C_1im][Ntf_2]$ to $[C_4C_1im][Ntf_2]$ the distributions start to encompass larger aggregates, with some islands as big as 25 and 100 tails observed for $[C_3C_1im][Ntf_2]$ and $[C_4C_1im][Ntf_2]$, respectively. Nevertheless, the highest probabilities always remain on the side of the smallest aggregates. When the next member of the IL series is considered, $[C_5C_1im][Ntf_2]$, a large distribution shift can be observed: the monotonic (decay-like) distributions observed before are replaced by a distribution with two non-negligible parts comprising small aggregates (1−20 tails) and one containing large aggregates (140−190 tails). This threshold corresponds to the appearance of the prepeak (shoulder) in the X-ray diffraction data,[34] or to other trend shifts in some properties along the $[C_nC_1im][Ntf_2]$ series.[33] It must be stressed that none of the aggregates observed in $[C_5C_1im][Ntf_2]$ comprise all the chains contained in the simulation box, and that most of the time most aggregates are not able to percolate the entire simulation box—albeit being very large islands they are still not able to form a second continuous mesophase (cf. discussion on the size and shape of the aggregates below). The next member of the series, $[C_6C_1im][Ntf_2]$, represents the definite shift toward large aggregates. However, most of these aggregates still do not comprise all tails (a few of them separate from time to time from to form small satellite islands) and full percolation is still achieved only part of the time. Finally, from $[C_7C_1im][Ntf_2]$ to $[C_{10}C_1im][Ntf_2]$, the distributions start to be completely shifted toward aggregates with all (or almost all) tails and the second continuous subphase percolates the whole simulation box during the entire production runs. It must be stressed that the present aggregation analyses are based on empirical (albeit carefully chosen) criteria and that the percolation thresholds just described can be slightly different if one adopts more stringent or more relaxed aggregation conditions. Nevertheless, this analysis shows a large shift in the aggregate distribution as one moves along the $[C_nC_1im][Ntf_2]$ series that is consistent with several sources of experimental and modeling data that has accumulated in recent years.

dx.doi.org/10.1021/jp409987d | J. Phys. Chem. B 2014, 118, 567−576

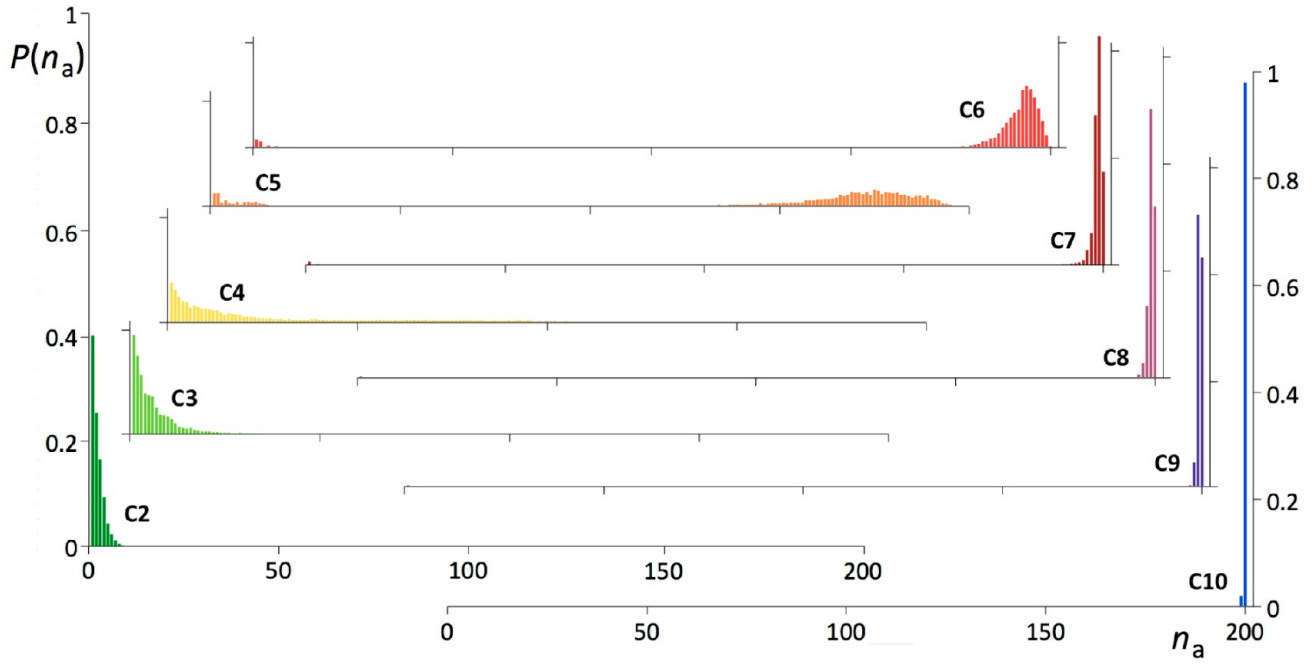

Figure 5. Discrete probability distribution of nonpolar aggregate sizes, $P(n_a)$, as a function of aggregate size number, n_a, for all ILs in the studied $[C_nC_1im][Ntf_2]$ homologous series.

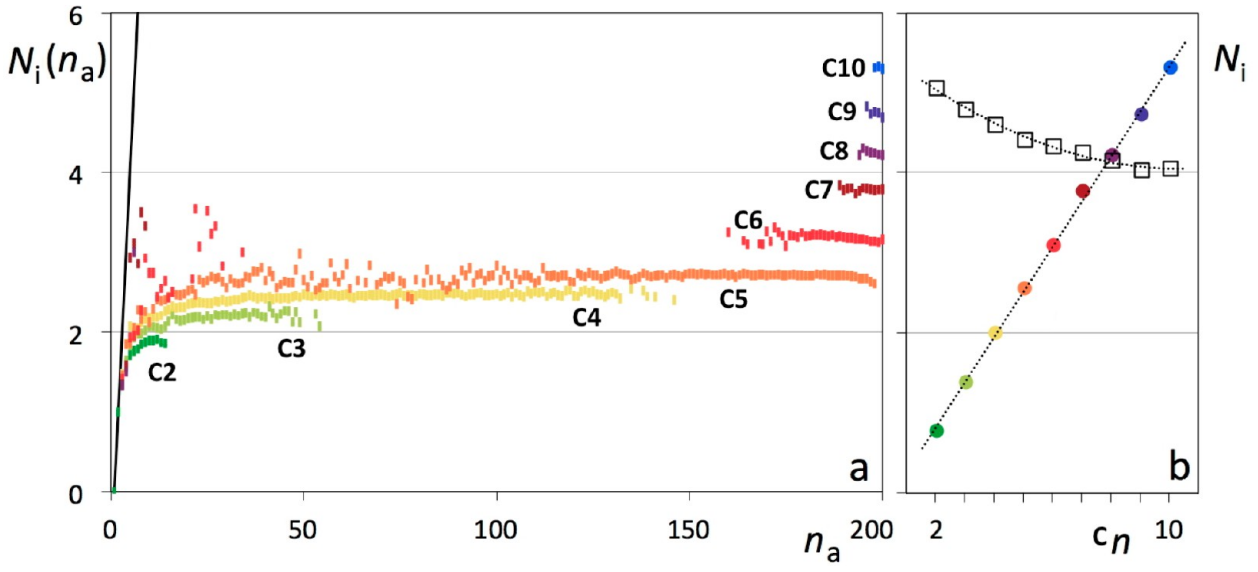

Figure 6. (a) Number of contact neighbors, $N_i(n_a)$, as a function of aggregate size number, n_a, for all tail aggregates in the studied $[C_nC_1im][Ntf_2]$ homologous series. (b) average size of contact neighbors, N_i, in the polar network (empty squares) or in the tail aggregates (filled color circles) as a function of alkyl side chain length, C_n.

The next parameter to be considered is the number of neighbors of a given ion or tail. This can be calculated as a function of the aggregate size that contains that given ion or tail, $N_i(n_a)$ or as an average number for the entire simulation box. N_i. Figure 5 represents both quantities for all studied ILs. In the case of the polar network, there is most of the time only one aggregate that contains all ions, which means that $N_i(\sim 200) = N_i$ and all other $N_i(\sim 200)$ values are simply not calculable due to insufficient statistics. In the case of the tail aggregates $N_i(n_a)$ values are only listed when the corresponding aggregate size distribution warrants such calculation.

For the polar network, the total number of neighbors N_i varies between a bit above 5 (for $[C_2C_1im][Ntf_2]$) and 4 (for $[C_{10}C_1im][Ntf_2]$). The N_i value decrease in a regular decay-like fashion along the series and seem to be reaching a more or less constant value (4) for the longer members of the series. These results are consistent with the progressive swelling and partial breakdown of the polar network as it tries to accommodate progressively larger nonpolar domains. The fact that it remains continuous (no polar fragments were found during the aggregation analyses) also suggests why the number of neighbors will tend to stabilize at some point along the series.

In the case of tail aggregates, one can conduct a much richer analysis.

For $[C_2C_1im][Ntf_2]$, the number of neighbors of a given tail varies between 0 (when it is an isolated tail) and around 2 when

dx.doi.org/10.1021/jp409987d | J. Phys. Chem. B 2014, 118, 567−576

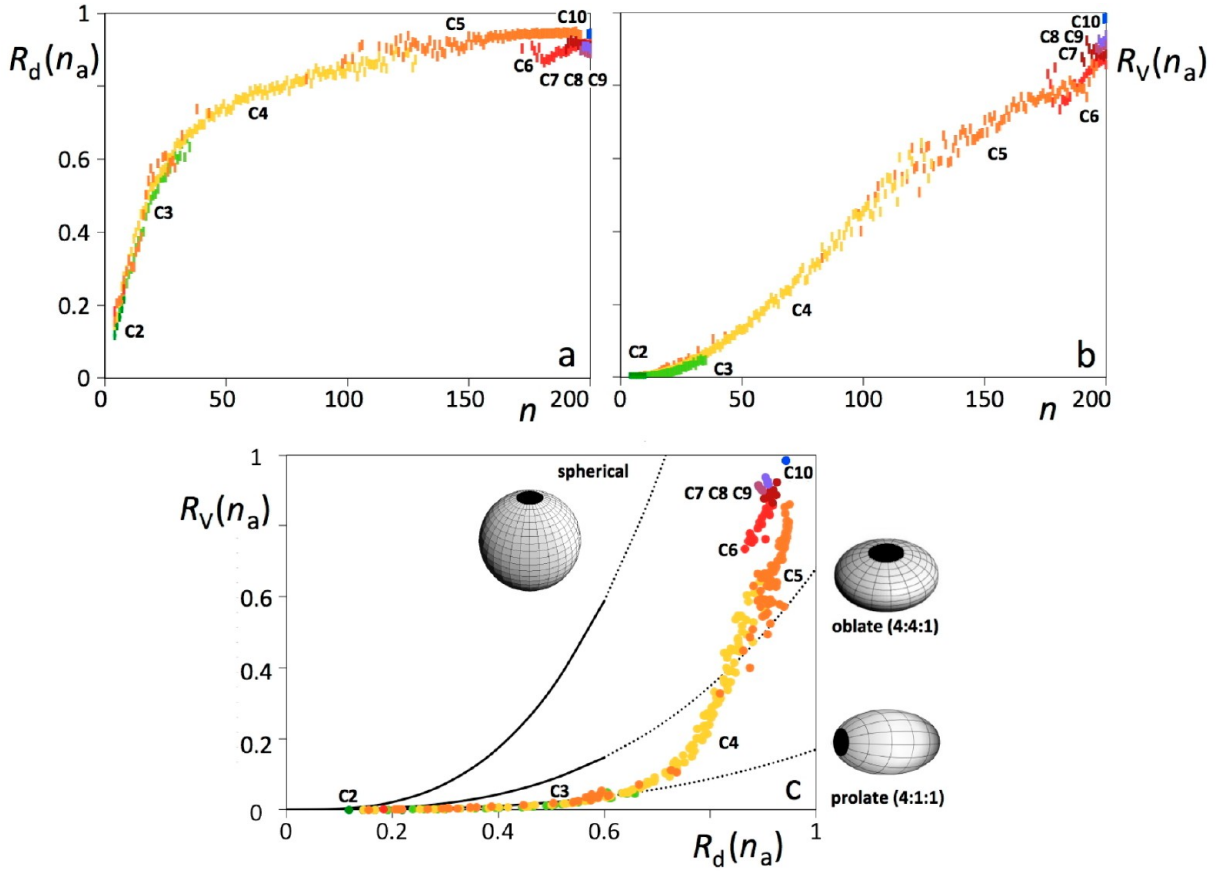

Figure 7. (a) Maximum aggregate length to box diagonal ratio, $R_d(n_a)$, as a function of aggregate size number, n_a, for all tail aggregates in the studied $[C_nC_1im][Ntf_2]$ homologous series. (b) Aggregate volume to box volume ratio, $R_V(n_a)$, as a function of aggregate size number, n_a, for all tail aggregates in the studied $[C_nC_1im][Ntf_2]$ homologous series. (c) $R_V(n_a)$ as a function of $R_d(n_a)$ for all tail aggregates in the studied $[C_nC_1im][Ntf_2]$ homologous series. The black lines represent the volume to maximum length relations for spheres, oblate ellipsoids and prolate ellipsoids (as depicted in the inset schematic figures).

the small tail is incorporated in small aggregates with a few (up to around 10) other tails. This means that in those small islands the tails are not all interconnected forming globular clusters (in that case the number of neighbors would be the size of the aggregate minus 1, along the black line depicted on the left side of Figure 6) but rather arranged in a more side-by-side fashion. The average number of neighbors for $[C_2C_1im][Ntf_2]$ is below 1, reflecting the large proportion of isolated tails in this particular IL.

In the case of $[C_3C_1im][Ntf_2]$ and $[C_4C_1im][Ntf_2]$, the aggregate sizes increase, but the number of neighbors remain slightly above 2 for $[C_3C_1im][Ntf_2]$ tail aggregates with sizes between 10 and 50 (most of these below 25, cf. Figure 6) and around 2.5 for $[C_4C_1im][Ntf_2]$ tail aggregates with sizes between 50 and 120 (most of these below 100, cf. Figure 6). The rather low numbers of aggregates (one tail is surrounded by just two or three other tails in aggregates that contain tens of other tails), suggest again a more side-to-side (elongated) arrangement of the tails in the aggregate than a more interconnected (globular) one. As the alkyl side chains increase (and the distributions of aggregates shift past the percolation threshold to much larger aggregates encompassing almost all tails within the simulation boxes), the number of neighbors per tail increases in a extremely regular (almost linear) fashion. Moreover from $[C_5C_1im][Ntf_2]$ onward, the number of neighbors as a function of the aggregate size is almost constant and the corresponding average reflects that value, $N_i(n_a) \approx N_i$. The increasing N_i value reflects on one hand the fact that longer tails can have more contact points with nearby chains simply because they are longer. On the other hand, as the nonpolar domains start to get larger, the side-by-side orientation that is favored in the smaller elongated aggregates can be extended in more than one direction after the percolation limit is achieved: side-by-side tails in one dimension (row) means two neighbors per tail; side-by-side tails in two dimensions (e.g., in a loose hexagonal packing) can easily mean up to six neighbors.

The final set of parameters to be investigated are related to the length and volume of the aggregates, $R_d(n_a)$ and $R_V(n_a)$, as a function of their size (number of tails). Since the polar network is continuous and percolates the entire simulation box for all studied ILs, this analysis is restricted to the nonpolar aggregates. In Figure 7 are represented (a) the ratio between the longest distance between two tails belonging to the same aggregate of size n_a and the diagonal of the simulation box, $R_d(n_a)$, as a function of n_a; (b) the ratio between the volume of an aggregate of size n_a and the volume of the simulation box, $R_V(n_a)$, as a function of n_a; and (c) the relation between $R_d(n_a)$ and $R_V(n_a)$.

Figure 7a,b shows that, although the information is not available for all aggregate sizes for each IL along the series (there are no aggregates larger than 10 for $[C_2C_1im][Ntf_2]$; there are no aggregates smaller than 195 for $[C_{10}C_1im][Ntf_2]$), and although the nature of the aggregates is being changed (the

dx.doi.org/10.1021/jp409987d | J. Phys. Chem. B 2014, 118, 567−576

length of the tails is slowly increasing), it is nevertheless possible to build a more or less consistent trend by "stitching" together information from different ILs along the series. One of the most obvious observations that can be taken by comparing Figures 7a and 7b is that, for smaller aggregates (n_a < 50), the maximum length of an aggregate increases much more rapidly with aggregate size than its volume. This means that smaller aggregates tend to be elongated (which corroborates the number of neighbors data), a fact that can be seen in the bottom of Figure 7c, where for the smaller aggregates (C2, C3, and smaller C4 data) the $R_V(n_a)$ versus $R_d(n_a)$ values are comparable to the volume versus length relation of a prolate (4:1:1 axes ratios) ellipsoid. When the size of the aggregates becomes greater than n_a = 50, the increase in length with the size of the aggregate starts to be less pronounced (cf. Figure 7a), whereas the increase in volume maintains its previous trend. This means that for intermediate-sized aggregates (50 < n_a < 180), most common for $[C_4C_1im][Ntf_2]$ and $[C_5C_1im][Ntf_2]$, the arrangement of the tails inside the aggregates starts to be more interconnected (more than two neighboring tails per tail, cf. Figure 6a) and the shape of the aggregate moves from prolate-like shapes to more oblate-like ones.

It must be stressed at this point that the trends depicted in Figure 7c representing the volume to maximum length relations in spheroid objects (black lines denoting spheres and ellipsoids) are just guidelines to help understand the approximate shapes of aggregates with a given $R_d(n_a)$ to $R_V(n_a)$ relation. The 1:4 ratio between the main axes of the oblate and prolate ellipsoids was empirically selected in order to have a match between the shape of prolate ellipsoids and the $R_d(n_a)$ and $R_V(n_a)$ data for aggregates with n_a < 50. Moreover, the black lines for the spheroid objects become dotted at a maximum length value of $(1/3)^{(1/2)} \approx 0.6$. This value marks the point at which the maximum length of the spheroid objects reach the size of the side of the simulation box. While the volume/length relations of the spheroids can still be calculated beyond this point, their comparison to $R_d(n_a)$ and $R_V(n_a)$ values must be progressively more cautious simply because the volume of aggregates will be limited by the boundary conditions imposed by the simulation box itself.

Finally, for very large aggregates (170 < n_a < 200), i.e., those containing most of the tails included in the simulation box, there is a sort of deviation in the $R_d(n_a)$ and $R_V(n_a)$ trends, which is visible specially in Figure.7c when one considers the $[C_5C_1im][Ntf_2]$ and $[C_6C_1im][Ntf_2]$ data. In these cases, it seems that the volume to length ratio increases suddenly and this can be explained by the fact that the bicontinuous phase starts to form from $[C_6C_1im][Ntf_2]$ onward—the polar network starts to be intermeshed with the nonpolar continuous domain. Since the volume of the later is estimated taking into account only 26 points at the aggregate surface, part of the polar network will be also included in the aggregate volume. This effect will be much more important after the percolation of the nonpolar domains and the above-mentioned deviation can be understood as another sign of the structural transition that occurs around $[C_5C_1im][Ntf_2]$.

CONCLUSIONS

This extensive and systematic MD study tried to reconcile and extend different aspects related to the structural shifts that occur along the $[C_nC_1im][Ntf_2]$ homologous series as the alkyl side chains become progressively larger. Large simulation boxes containing 1600 ion pairs (almost 100000 explicit atoms) were used to estimate the corresponding $g(r)$ and $S(q)$ functions along the series and the results enabled to rationalize and confirm the relation between the existence of a low-q $S(q)$ peak and the formation of a continuous nonpolar mesophase from $[C_6C_1im][Ntf_2]$ onward. The structural changes that occur in the polar network along the series were also considered, specially taking into account the trends observed for the intermediate-q $S(q)$ peak and its correspondence to the spacing between polar network shells in the corresponding $g(r)$ functions. The following aggregate analyses revealed that in the smaller members (C2–C4) of the IL series, the corresponding nonpolar (tail) aggregates form elongated clusters with an increasing number of tails per aggregate, that become more oblate around $[C_5C_1im][Ntf_2]$ and start to percolate the IL as a second continuous subphase from $[C_6C_1im][Ntf_2]$ onward. Finally, the number of counterion first-shell neighbors of a given ion decreases from around 5 to 4 along the $[C_nC_1im][Ntf_2]$ series, confirming that the polar network is partially broken to allow the formation of the nonpolar subphase. On the other hand, the number of contact neighbors in the tail aggregates increases along the series from an average value smaller than 1 in $[C_nC_1im][Ntf_2]$ to a value larger than 5 in $[C_{10}C_1im][Ntf_2]$. The sponge-like structure of both subphases (and the length of the tails in the case of the nonpolar domains) can easily accommodate such number of neighbors.

AUTHOR INFORMATION

Corresponding Author

*E-mail: jnlopes@ist.utl.pt; website: http://web.ist.utl.pt/jnlopes.

Author Contributions

K.S. and C.B. contributed equally to this work as first authors.

Notes

The authors declare no competing financial interest.

ACKNOWLEDGMENTS

Financial support provided by Fundação para a Ciência e Tecnologia (FCT) through projects FCT-ANR/CTM-NAN/0135/2012, PTDC/CTM-NAN/121274/2010 and PEst-OE/QUI/UI0100/2013. K.S. and C.B. acknowledge postdoctoral grants SFRH/BPD/38339/2007 and SFRH/BPD/43346/2008, respectively.

REFERENCES

(1) Urahata, S. M.; Ribeiro, M. C. C. Structure of ionic liquids of 1-alkyl-3-methylimidazolium cations: A systematic computer simulation study. *J. Chem. Phys.* **2004**, *120*, 1855–1863.

(2) Wang, Y.; Voth, G. A. Unique Spatial Heterogeneity in Ionic Liquids. *J. Am. Chem. Soc.* **2005**, *127*, 12192–12193.

(3) Pádua, A. A. H.; Canongia Lopes, J. N. Nanostructural Organization in Ionic Liquids. *J. Phys. Chem. B* **2006**, *110*, 3330–3335.

(4) Triolo, A.; Russina, O.; Bleif, H.; Di Cola, E. Nanoscale Segregation in Room Temperature Ionic Liquids. *J. Phys. Chem. B* **2007**, *111*, 4641–4644.

(5) Annapureddy, H. V. R.; Kashyap, H. K.; De Biase, P. M.; Margulis, C. J. What is the Origin of the Prepeak in the X-ray Scattering of Imidazolium-Based Room-Temperature Ionic Liquids? *J. Phys. Chem. B* **2010**, *114*, 16838–16846.

(6) Bhargava, B. L.; Devane, R.; Klein, M. L.; Balasubramanian, S. Nanoscale organization in room temperature ionic liquids: a coarse grained molecular dynamics simulation study. *Soft Matter* **2007**, *3*, 1395–1400.

(7) Castner, E. W.; Wishart, J. F. Spotlight on ionic liquids. *J. Chem. Phys.* **2010**, *132*, 120901−1−120901−9.
(8) Hardacre, C.; Holbrey, J. D.; Mullan, C. L; Youngs, T. G. A.; Bowron, D. T. Small angle neutron scattering from 1-alkyl-3-methylimidazolium hexafluorophosphate ionic liquids ($[C_n mim][PF_6]$, n = 4, 6, and 8). *J. Chem. Phys.* **2010**, *133*, 74510−74517.
(9) Kashyap, H. K.; Santos, C. S.; Sanjeeva Murthy, N.; Hettige, J. J.; Kerr, K.; Ramati, S.; Gwon, J.; Gohdo, M.; Lall-Ramnarine, S. I.; Wishart, J. F.; Margulis, C. J.; Castner, E. W., Jr. Structure of 1-Alkyl-1-methylpyrrolidinium Bis(trifluoromethylsulfonyl)amide Ionic Liquids with Linear, Branched, and Cyclic Alkyl Groups. *J. Phys. Chem. B* **2013**, DOI: 10.1021/jp403518j.
(10) Kashyap, H. K.; Hettige, J. J.; Annapureddy, H. V. R.; Margulis, C. J. SAXS anti-peaks reveal the length-scales of dual positive−negative and polar−apolar ordering in room-temperature ionic liquids. *Chem. Commun.* **2012**, *48*, 5103−5105.
(11) Borodin, O.; Smith, G. D. Structure and Dynamics of *N*-Methyl-*N*-propylpyrrolidinium Bis(trifluoromethanesulfonyl)imide Ionic Liquid from Molecular Dynamics Simulations. *J. Phys. Chem. B* **2006**, *110*, 11481−11490.
(12) Siqueira, L. J. A.; Ribeiro, M. C. C. Charge ordering and intermediate range order in ammonium ionic liquids. *J. Chem. Phys.* **2011**, *135*, 204506−1−204506−7.
(13) Yamaguchi, T.; Mikawa, K.; Koda, S.; Fujii, K.; Endo, H.; Shibayama, M.; Hamano, H.; Umebayashi, Y. Relationship between mesoscale dynamics and shear relaxation of ionic liquids with long alkyl chain. *J. Chem. Phys.* **2012**, *137*, 104511−1−104511−7.
(14) Borodin, O.; Gorecki, W.; Smith, G. D.; Armand, M. Molecular Dynamics Simulation and Pulsed-Field Gradient NMR Studies of Bis(fluorosulfonyl)imide (FSI) and Bis[(trifluoromethyl)sulfonyl]-imide (TFSI)-Based Ionic Liquids. *J. Phys. Chem. B* **2010**, *114*, 6786−6798.
(15) Gontrani, L.; Russina, O.; Lo Celso, F.; Caminiti, R.; Annat, G.; Triolo, A. Liquid Structure of Trihexyltetradecylphosphonium Chloride at Ambient Temperature: An X-ray Scattering and Simulation Study. *J. Phys. Chem. B* **2009**, *113*, 9235−9240.
(16) Hettige, J. J.; Kashyap, H. K.; Annapureddy, H. V. R.; Margulis, C. J. Anions, the Reporters of Structure in Ionic Liquids. *J. Phys. Chem. Lett.* **2013**, *4*, 105−110.
(17) Song, X. D.; Hamano, H.; Minofar, B.; Kanzaki, R.; Fujii, K.; Kameda, Y.; Kohara, S.; Watanabe, M.; Ishiguro, S.; Umebayashi, Y. Structural Heterogeneity and Unique Distorted Hydrogen Bonding in Primary Ammonium Nitrate Ionic Liquids Studied by High-Energy X-ray Diffraction Experiments and MD Simulations. *J. Phys. Chem. B* **2012**, *116*, 2801−2813.
(18) Umebayashi, Y.; Hamano, H.; Tsuzuki, S.; Canongia Lopes, J. N.; Pádua, A. A. H.; Kameda, Y.; Kohara, S.; Yamaguchi, T.; Fujii, K.; Ishiguro, S. Dependence of the Conformational Isomerism in 1-*n*-Butyl-3-methylimidazolium Ionic Liquids on the Nature of the Halide Anion. *J. Phys. Chem. B* **2010**, *114*, 11715−11724.
(19) Rocha, M. A. A.; Lima, C. F. R. A. C.; Gomes, L. R.; Schröder, B.; Coutinho, J. A. P.; Marrucho, I. M.; Esperança, J. M. S. S.; Rebelo, L. P. N.; Shimizu, K.; Canongia Lopes, J. N.; Santos, L. M. N. B. F. High-Accuracy Vapor Pressure Data of the Extended $[C_nC_1im][Ntf_2]$ Ionic Liquid Series: Trend Changes and Structural Shifts. *J. Phys. Chem. B* **2011**, *115*, 10919−10926.
(20) Hardacre, C.; Holbrey, J. D.; Nieuwenhuyzen, M.; Youngs, T. G. A. Structure and Solvation in Ionic Liquids. *Acc. Chem. Res.* **2007**, *40*, 1146−1155.
(21) Castner, E. W.; Wishart, J. F.; Shirota, H. Intermolecular Dynamics, Interactions, and Solvation in Ionic Liquids. *Acc. Chem. Res.* **2007**, *40*, 1217−1227.
(22) Canongia Lopes, J. N.; Deschamps, J.; Pádua, A. A. H. Modeling Ionic Liquids Using a Systematic All-Atom Force Field. *J. Phys. Chem. B* **2004**, *108*, 2038−2047.
(23) Canongia Lopes, J. N.; Pádua, A. A. H. Molecular Force Field for Ionic Liquids Composed of Triflate or Bistriflylimide Anions. *J. Phys. Chem. B* **2004**, *108*, 16893−16898.
(24) Canongia Lopes, J. N.; Pádua, A. A. H. CL&P: A generic and systematic force field for ionic liquids modeling. *Theor. Chem. Acc.* **2012**, *131*, 1129.
(25) Jorgensen, W. L.; Maxwell, D. S.; Tirado-Rives, J. Development and Testing of the OPLS All-Atom Force Field on Conformational Energetics and Properties of Organic Liquids. *J. Am. Chem. Soc.* **1996**, *118*, 11225−11236.
(26) Smith, W.; Forester, T. R. *The DL_POLY Package of Molecular Simulation Routines (v.2.2)*; The Council for The Central Laboratory of Research Councils; Daresbury Laboratory: Warrington, U.K., 2006.
(27) Shimizu, K.; Bernardes, C. E. S.; Triolo, A.; Canongia Lopes, J. N. Nano-segregation in ionic liquids: scorpions and vanishing chains. *Phys. Chem. Chem. Phys.* **2013**, *15*, 16256−16262.
(28) Brown, P. J.; Fox, A. G.; Maslen, E. N.; O'Keefe, M. A.; Willis, T. M. *International Tables for Crystallography*, Prince, E., Ed.; International Union of Crystallography: Dordrecht, The Netherlands, 2004; Vol. *C*, p 554−595.
(29) Lorch, E. Neutron diffraction by germania, silica and radiation-damaged silica glasses. *J. Phys. C: Solid State Phys.* **1969**, *2*, 229−237.
(30) Bernardes, C. E. S.; Minas da Piedade, M. E.; Canongia Lopes, J. N. The Structure of Aqueous Solutions of a Hydrophilic Ionic Liquid: The Full Concentration Range of 1-Ethyl-3-methylimidazolium Ethylsulfate and Water. *J. Phys. Chem. B* **2011**, *115*, 2067−2074.
(31) Raju, S. G.; Balasubramanian, S. Role of Cation Symmetry in Intermolecular Structure and Dynamics of Room Temperature Ionic Liquids: Simulation Studies. *J. Phys. Chem. B* **2010**, *114*, 6455−6463.
(32) Bodo, E.; Gontrani, L.; Caminiti, R.; Plechkova, N. V.; Seddon, K. R.; Triolo, A. Structural Properties of 1-Alkyl-3-methylimidazolium Bis{(trifluoromethyl)sulfonyl}amide Ionic Liquids: X-ray Diffraction Data and Molecular Dynamics Simulations. *J. Phys. Chem. B* **2010**, *114*, 16398−16407.
(33) Rocha, M. A. A.; Neves, C. M. S. S.; Freire, M. G.; Russina, O.; Triolo, A.; Coutinho, J. A. P.; Santos, L. M. N. B. F. Alkylimidazolium Based Ionic Liquids: Impact of Cation Symmetry on Their Nanoscale Structural Organization. *J. Phys. Chem. B* **2013**, *117*, 10889−10897.
(34) Russina, O.; Triolo, A.; Gontrani, L.; Caminiti, R.; Xiao, D.; Hines, L. G., Jr; Bartsch, R. A.; Quitevis, E. L.; Plechkova, N.; Seddon, K. R. Morphology and intermolecular dynamics of 1-alkyl-3-methylimidazolium bis{(trifluoromethane)sulfonyl}amide ionic liquids: structural and dynamic evidence of nanoscale segregation. *J. Phys.: Condens. Matter* **2009**, *21*, 424121-1−424121-9.
(35) Pádua, A. A. H.; Costa Gomes, M. F.; Canongia Lopes, J. N. Molecular Solutes in Ionic Liquids: A Structural Perspective. *Acc. Chem. Res.* **2007**, *40*, 1087−1096.